


Article

Generating 1 km Spatially Seamless and Temporally Continuous Air Temperature Based on Deep Learning over Yangtze River Basin, China

Rui Li ¹, Tailai Huang ², Yu Song ², Shuzhe Huang ^{3,*}  and Xiang Zhang ^{2,3}

¹ Changjiang Wuhan Waterway Bureau, Wuhan 430014, China; ray_hdj@yeah.net

² National Engineering Research Center of Geographic Information System, School of Geography and Information Engineering, China University of Geosciences, Wuhan 430074, China; cug_gis_htl@163.com (T.H.); Casablanca_yu@163.com (Y.S.); zhangxiang76@cug.edu.cn (X.Z.)

³ State Key Laboratory of Information Engineering in Surveying, Mapping, and Remote Sensing (LIESMARS), Wuhan University, Wuhan 430079, China

* Correspondence: szhuang@whu.edu.cn; Tel.: +86-18038021202

Abstract: Air temperature is one of the most essential variables in understanding global warming as well as variations of climate, hydrology, and eco-systems. However, current products and assimilation approaches alone can provide temperature data with high resolution, high spatio-temporal continuity, and high accuracy simultaneously (refer to 3H data). To explore this kind of potential, we proposed an integrated temperature downscaling framework by fusing multiple remotely sent, model-based, and in-situ datasets, which was inspired by point-surface data fusion and deep learning. First, all of the predictor variables were processed to maintain spatial seamlessness and temporal continuity. Then, a deep belief neural network was applied to downscale temperature with a spatial resolution of 1 km. To further enhance the model performance, calibration techniques were adopted by integrating station-based data. The results of the validation over the Yangtze River Basin indicated that the average Pearson correlation coefficient, RMSE, and MAE of downscaled temperature achieved 0.983, 1.96 °C, and 1.57 °C, respectively. After calibration, the RMSE and MAE were further decreased by ~20%. In general, the results and comparative analysis confirmed the effectiveness of the framework for generating 3H temperature datasets, which would be valuable for earth science studies.

Keywords: temperature downscaling; deep learning; point-surface fusion; Yangtze River basin



Citation: Li, R.; Huang, T.; Song, Y.; Huang, S.; Zhang, X. Generating 1 km Spatially Seamless and Temporally Continuous Air Temperature Based on Deep Learning over Yangtze River Basin, China. *Remote Sens.* **2021**, *13*, 3904. <https://doi.org/10.3390/rs13193904>

Academic Editor: Pavel Kishcha

Received: 30 August 2021

Accepted: 26 September 2021

Published: 29 September 2021

Publisher's Note: MDPI stays neutral with regard to jurisdictional claims in published maps and institutional affiliations.



Copyright: © 2021 by the authors. Licensee MDPI, Basel, Switzerland. This article is an open access article distributed under the terms and conditions of the Creative Commons Attribution (CC BY) license (<https://creativecommons.org/licenses/by/4.0/>).

1. Introduction

Surface air temperature is one of the most critical land surface variables in the fields of hydrology, meteorology, earth system sciences, and also plays a vital role in climate change, natural disasters, and human health [1,2]. Global warming (i.e., increasing global temperature) in recent decades has attracted scientists' attention since it has led to dramatic changes in the global eco-system, which has induced rise of the sea's surface level, the growth of extreme events (e.g., floods and droughts), and ultimately damages to human lives [3–7]. Over the last few decades, there are two most direct sources for acquiring air temperature data. On the one hand, in-situ weather stations are superior in providing long-term, stable, and accurate temperature recordings. However, their costly maintenance and sparse distribution are the major limitations for their application in regional or global earth science research [8,9]. On the other hand, a variety of data assimilation and reanalysis approaches have been developed to produce large scale assimilated products such as the Japanese 55-year Reanalysis Project (JRA-55), the Global Land Data Assimilation System (GLDAS), the NCEP/DOE Reanalysis 2 Project (NNRP-2), and the ERA-5 reanalysis product [10–13]. Although these assimilated products are capable of providing both regional and global data, the coarse resolution and relatively low accuracy usually limits their use for fine impact assessment and decision making [14,15].

Generally speaking, current point-wise ground observations and assimilated products have diverse but also opposite advantages in providing air temperature data. However, neither of them alone can provide a temperature product which has high resolution, high spatio-temporal continuity (i.e., spatially seamless and temporally continuous), and high accuracy simultaneously. This kind of temperature product is defined as 3H data in this study. 3H temperature products are of great importance for investigating local to global changes and mechanisms of various ecological and hydrological processes such as snow melting and the prediction of streamflow and evapotranspiration [16,17]. Therefore, under a changing environment, it is still urgently necessary to utilize downscaling and data fusion techniques to generate 3H temperature data.

Temperature downscaling can be generally classified into two methods, namely dynamical downscaling and statistical downscaling [18]. Dynamical downscaling applies a numerical weather model (e.g., weather research and forecasting model) and regional climate model (e.g., regional climate model) to produce high resolution climate variables by simulating physical processes of the coupled land-atmosphere system [19,20]. For instance, Zhou et al. [21] developed downscaled temperature by using the providing regional climates for impacts studies (PRECIS) model. The results indicated that PRECIS had excellent performance in capturing temperature spatial patterns. Hou et al. [22] used an energy balance Bowen ratio model to retrieve air temperature, and the mean error was approximately 2.21 °C. Nevertheless, these models are often limited by complicated parameters, intensive computational resources, and non-transferability between regions [23,24].

Compared to dynamical downscaling, statistical downscaling can establish the statistical relationship between air temperature and other related climate or geographical variables [25,26]. For instance, Li et al. [27] applied the geographical weighted regression (GWR) method to generate 1 km air temperature over the conterminous United States by taking land surface temperature (LST) and elevation as explanatory variables. Recently, machine learning methods have also been widely adopted in data fusion [28,29]. Popular algorithms include the random forest, multiple linear regression, and artificial neural network methods. Zhang et al. [30] adopted the cubist regression, gradient boosting, and random forest methods to integrate eight types of land assimilation products and produced 1 km long-term temperature in the Tibetan Plateau. Additionally, Rao et al. [31] utilized cubist model to estimate daily temperature at 0.05° using LST and top-of-atmosphere radiation products.

Despite the great achievement by aforementioned researchers, there are still some limitations in producing 3H temperature. The statistical downscaling usually constructs the linear or non-linear relationship between air temperature and related factors. However, some commonly used remotely sensed variables (e.g., LST, NDVI) are not always spatially seamless and temporally continuous due to the contamination of clouds and atmospheric condition. To this point, the downscaled temperature is also difficult to achieve the 3H goal [32–34]. In addition, although previous studies have generated air temperature with acceptable results, reliable calibration techniques are still required to substantially improve the accuracy of downscaled temperature. Since station-based observations are considered to be the most accurate, the integration of ground data in bias correction is also promising for generating high accuracy temperature [35,36]. Moreover, with the arrival of big data era, deep learning has made great impact in various fields due to its powerful capability in simulating the non-linear relationship [37,38]. However, the applications of deep learning in the fields of hydrology, climate, and earth science are still in an infant stage. Therefore, whether deep learning can also exhibit excellent performance in temperature downscaling is an interesting question to explore.

To address the aforementioned issue, the main objective of this study is to develop an air temperature downscaling framework by combining point-surface data fusion and deep learning method. The proposed framework is designed to generate high resolution (1 km), high spatio-temporal continuity (cloud-free and daily), and high accuracy (high correlation and low error) temperature product. In this case, the generated 3H temperature product

will help better understanding of the variations in hydrology, climate, and eco-system under the changing environment.

2. Study Area and Data

2.1. Study Area

The Yangtze River Basin (YRB) was selected as the study area, which is the third largest river in the world (Figure 1). Covering an area about 1.8 million km² which occupies nearly 18.8% of the extent of entire China mainland, YRB concentrates almost one third of the total population in China. Additionally, YRB also shows substantial spatial heterogeneity of land-cover types. With higher altitude in the upper region and lower altitudes in the midstream and downstream, the topography of YRB indicates a three-step ladder distribution, flowing through mountains, plateaus, basins, hills, and plains. To this point, the climate, meteorological and hydrological characteristics, and land covers in YRB are extremely complicated. Specifically, the distribution of annual precipitation is uneven, ranging from 500 mm in the west to 2500 mm in the east. The feature of temperature in YRB is formed under the influence of multiple factors such as solar radiation energy, East Asia atmospheric circulation, and the topography of Qinghai-Tibet Plateau. The annual mean temperature in YRB represents a trend of high temperatures in the east and low temperatures in the west. Due to the impact of different topography, the Sichuan Basin, Yunnan-Guizhou Plateau, and Jinsha River Valley have formed enclosed high and low temperature central areas. Over the last few decades, global warming has greatly influenced the hydrological cycle in YRB. For instance, Li et al. [39] investigated that the intensity and frequency of extreme rainfall event have increased significantly with the increase of temperature. Chen et al. [40] concluded that the occurrence frequency and severity of droughts under global warming of 1.5 °C and floods under global warming of 2 °C indicated an upward trend in YRB. To this point, an all-weather high resolution air temperature dataset is of great significance to understand the variation and underlying mechanism of the modified hydrological cycle and natural disasters in YRB under the changing environment.

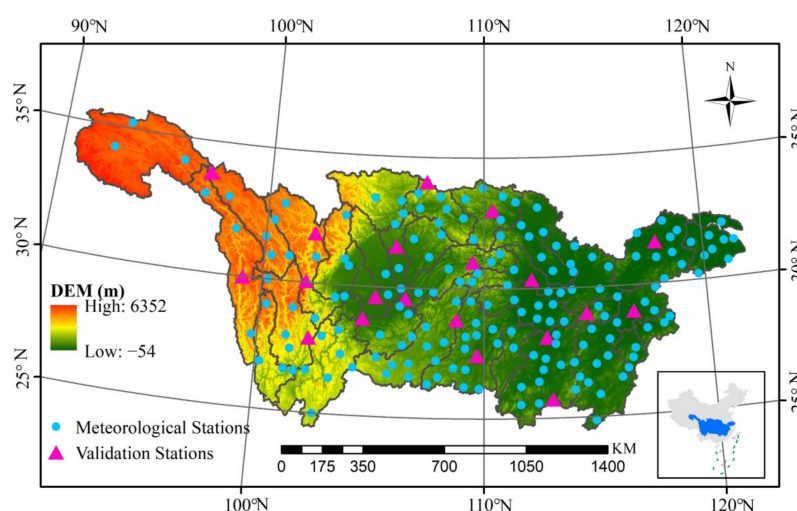


Figure 1. The geographical location of Yangtze River Basin. The blue points represent the meteorological stations used for model training while the purple triangles indicate the stations used for model validation.

2.2. Data

In this study, a total of three categories of datasets were adopted for temperature downscaling, which are elaborated in Table 1. The datasets can be classified as: (1) remotely

sensed data including MODIS and SRTM products, (2) model-based data including ERA-5 and TRIMS LST products, and (3) in-situ ground measurement from weather stations.

Table 1. The detailed information of three categories of products used in this study.

Category	Product	Variable	Spatial Resolution	Temporal Resolution
Remotely Sensed Products	MOD13A2	NDVI	1 km	16 Days
	SRTM	DEM	90 m	—
Model-based Products	ERA5	2 m Temperature Soil moisture Wind Speed Albedo	0.1°	Hourly
	TRIMS LST	LST	1 km	Daily
Ground Data	In-situ Station	Mean Temperature	—	Daily

2.2.1. Remotely Sensed Product

Moderate Resolution Imaging Spectroradiometer (MODIS) is the major instrument aboard Aqua and Terra satellite. Depending on the opposite transit direction of Aqua (south to north) and Terra (north to south), MODIS satellite can obtain global surface observations once or twice per day in 36 spectral bands. In this study, we selected NDVI as one of the predictors for temperature downscaling model. The temporal variation of NDVI is relatively stable compared to other highly time-varying variables such as land surface temperature. Therefore, we adopted MODIS vegetation index product (MOD13A2) which was collected from Application for Extracting and Exploring Analysis Ready Samples (AppEEARS). MOD13A2 Version 6 provides vegetation index values with a spatial resolution of 1 km and temporal resolution of 16 days, which can greatly reduce the proportions of pixels with missing values due to the cloud contamination and atmospheric conditions.

Additionally, we also collected global resampled Shuttle Radar Topography Mission (SRTM) digital elevation product with a spatial resolution of 90 m.

2.2.2. Model-Based Product

Previous researches have demonstrated that land surface temperature (LST) had strong positive relationship with air temperature and could be an effective variable in generating 3H temperature products [41,42]. However, current MODIS LST products (e.g., MOD11A1) fail to provide long-term spatially seamless LST data due to the cloud contamination and atmospheric pollution, which would further lead to the discontinuity of downscaled temperature data. To overcome this issue, we adopted a 1 km all weather Thermal and Reanalysis Integrating Moderate-resolution Spatial-seamless (TRIMS) LST product, which covers China mainland and its neighboring areas [43,44]. TRIMS LST was generated by a novel reanalysis and thermal infrared remote sensing data merging (RTM) method based on the decomposition model of LST series. And the dataset has been validated to be applicable for associated hydrological and meteorological studies with excellent performance compared with MODIS LST and other existing products [45].

Moreover, we introduced ERA-5 reanalysis product to provide 2 m model-based air temperature, forecast albedo, wind speed, and soil moisture. Developed by European Centre for Medium-Range Weather Forecasts (ECMWF), ERA-5 is the successor of previous ERA-Interim, which is the latest generation for providing global atmospheric, land and oceanic climate variables. ERA-5 assimilates various satellite data and in-situ ground measurements using 4D-Var data assimilation technique and produces datasets with a spatial resolution of 0.1°, which has been widely used in various fields of studies.

2.2.3. In-Situ Measurement

In-situ ground measurements of air temperature were acquired from China Meteorological Data Service Center (CMDSC). After the screening by the boundary of YRB, a total of 194 meteorological stations were selected as the sources of in-situ data. The location and distribution of in-situ stations can be observed at Figure 1. Higher density of stations is concentrated in the middle and lower regions of YRB while the distribution of stations in the upper region is relatively sparse. In this study, daily average air temperature is selected as the major downscaling factor.

3. Methods

3.1. Methodology

The proposed high resolution spatially seamless and temporally continuous temperature downscaling framework is shown in Figure 2. Generally, the methodology can be divided into three parts: (1) Data collection and preprocessing (Section 3.2); (2) deep learning based temperature downscaling (Section 3.3); (3) and bias correction for down-scaled temperature (Section 3.4). More detailed information about the methodology were outlined below.

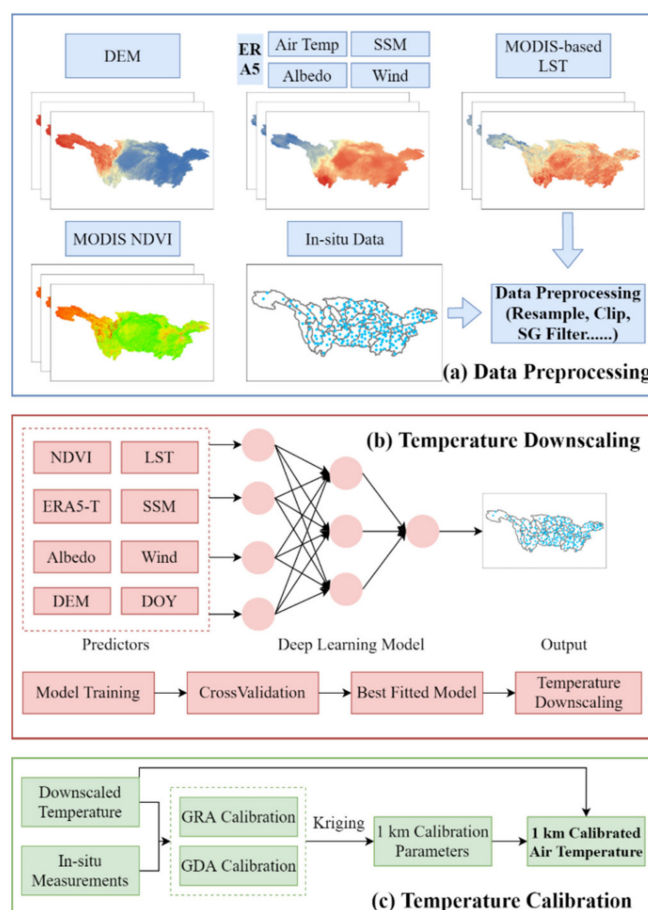


Figure 2. The methodology of temperature downscaling. The entire framework can be generally divided into three parts including (a) data preprocessing, (b) temperature downscaling, and (c) temperature calibration.

3.2. Data Preprocessing

In total, we collected multi-source datasets for the downscaling framework including remotely sensed, model-based, and in-situ products. Each of these products had diverse spatial and temporal resolution. Therefore, before the downscaling, necessary data prepro-

cessing operations (i.e., reprojection, resampling, clipping) should be completed to ensure the same extent and resolution.

Additionally, for NDVI products, although MOD13A2 had 16-day resolution, there were still some small proportions of pixels with missing or unreliable values. In order to provide seamless NDVI and further produce all-weather downscaled temperature, we utilized Savitzky-Golay (SG) filter method to reconstruct unreliable NDVI pixels [46,47]. SG filter uses a simplified high-order polynomial approximation sliding windows to smooth derivatives of a set of consecutive values [48]. The general equation of SG fitting process can be given as:

$$Y_j^* = \sum_{i=-m}^{i=m} \frac{C_i Y_{j+1}}{N} \quad (1)$$

where Y_j^* and Y_{j+1} are the smoothed and original NDVI, respectively. C_i is the coefficient calculated by SG filter and N is the number of convoluting integers. m is the size of half of smoothing window. Before the SG filtering, we introduced the pixel reliability files of MOD13A2 to identify the unreliable NDVI pixels. Specifically, the values of unreliable pixels were equal to 2 and 3 in the quality control files. Then, the unreliable values would be replaced by a linear interpolation method using the adjacent NDVI values, which can be given as follows:

$$N^0(i, t) = \begin{cases} aN(i, t-1) + bN(i, t+1), & R = 2, 3 \\ N(i, t), & R = 0, 1 \end{cases} \quad (2)$$

where R is the reliability value in the quality control file and $N(i, t)$ is the NDVI of the i^{th} pixel in the t^{th} time. $N^0(i, t)$ is the NDVI value after the judgment of Equation (2). After the linear interpolation, the SG filter process will begin.

3.3. Deep Learning Based Temperature Downscaling

There have been some studies demonstrated that deep learning models had effective capability of monitoring the non-linear relationship between different land surface variables. And deep belief network (DBN) has been shown to have excellent performance in the field of data fusion [26,49,50]. DBN is a Bayesian probability generation model which consists of multiple restricted Boltzmann machines (RBM) layers and one back-propagation (BP) layer [51]. The traditional structures of DBN and RBM are shown in Figure 3. An RBM is a two-layer neural network, which contains one hidden layer and one visible layer with full connection between two layers but no connection within each layer. Let v and h indicate the state of visible layer and hidden layer. v_i and h_i represent the i^{th} neuron of the corresponding layers, respectively. Then the equation of energy function of RBM can be given as follows:

$$E(v, h/\theta) = -\sum_{i=1}^m a_i v_i - \sum_{j=1}^n b_j h_j - \sum_{i=1}^m \sum_{j=1}^n v_i W_{ij} h_j \quad (3)$$

where $\theta = \{W_{ij}, a_i, b_j\}$ means the parameters to be estimated. To be specific, W represents the weight matrix while a and b denote the bias of visible neurons and hidden neurons, respectively. The training of DBN can be generally divided into two steps. First, the pre-training step starts from the input layer to the hidden layer of the last RBM network without supervision in order to study significant features from the independent variables. Then, the initialized parameters (i.e., weights and biases) will be further refined by the BP network to make the predicted values closer to the dependent variable.

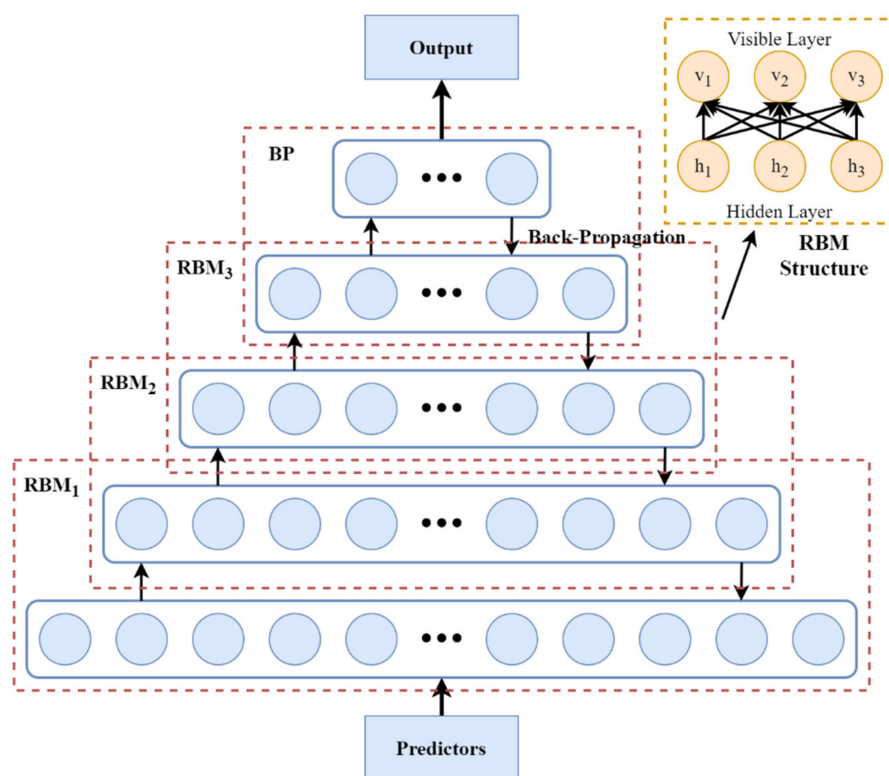


Figure 3. The structure of deep belief neural network.

In this study, a total of eight variables were regarded as the predictors for the DBN model including ERA-5 temperature, surface soil moisture, wind speed, albedo, LST, NDVI, DEM, and a time variable (i.e., DOY). All predictors were downsampled and resampled to 1 km spatial resolution so that the finally downsampled temperature could maintain high spatial resolution. The output variable of DBN was in-situ average air temperature. The downsampled model can be expressed as:

$$Temperature_{downsampled} = f(ERA5\ T, SSM, Wind, Albedo, LST, NDVI, DEM, DOY) \quad (4)$$

where $f(\cdot)$ is the DBN model. The study period was selected as the whole year of 2019 and there was a total of 194 meteorological stations in the study area. For each station, the input sample set has two dimensions of which the shape is 365×8 , indicating 365 days (one year) and 8 input variables. Therefore, all meteorological stations formed the sample set of $194 \times 365 \times 8$. Then all stations were randomly classified as training set, validation set, and test set with the ratio of 7:2:1. And cross validation was used to assess the performance of downscaling models. Finally, the selected best-fitted DBN model would be applied to other pixels with all predictors available and downsampled seamless and continuous temperature at 1 km resolution.

3.4. Bias Correction for Downsampled Temperature

The downsampled temperature based on DBN model still contains certain underestimation or overestimation against ground observations due to the error propagation from the resampling of coarse resolution products (e.g., ERA-5). Additionally, the heterogeneous distribution of model predictors may also affect the downscaling accuracy [52]. To further improve the accuracy of downsampled temperature and achieve the 3H goal, we introduced

two calibration strategies which were geographical ratio analysis (GRA) and geographical difference analysis (GDA) [53,54]. The equations of GRA and GDA were given as follows:

$$P_{corrected}(x) = P_{downscaled}(x) \times \sum_{i=1}^n \lambda_i \frac{P_{obs}(x_i)}{P_{downscaled}(x_i)} \quad (5)$$

$$P_{corrected}(x) = P_{downscaled}(x) + \sum_{i=1}^n \lambda_i (P_{obs}(x_i) - P_{downscaled}(x_i)) \quad (6)$$

where $P_{corrected}$, $P_{downscaled}$, and P_{obs} represent the calibrated, originally downscaled, and observed temperature at location x , respectively. λ is the weight at location x . Then, the ratio $P_{obs}/P_{downscaled}$ and the difference $P_{obs} - P_{downscaled}$ at in-situ stations would be interpolated to the entire study region with a spatial resolution of 1 km using ordinary Kriging algorithm. Finally, the interpolated calibration parameters would be compensated to the downscaled temperature to obtain calibrated high accuracy temperature data.

3.5. Statistical Metrics

A total of four statistical metrics were applied to evaluate the performance of downscaled temperature, including Pearson correlation coefficient (PCC), root mean squared error (RMSE), mean absolute error (MAE), and bias. The detailed information of these four metrics is listed in Table 2.

Table 2. The equations and detailed information of PCC, RMSE, bias, and MAE. P_i and M_i represent the i^{th} downscaled value and ground measurement, respectively. \bar{P} and \bar{M} indicate the average values of downscaled temperature and in-situ measurements. n is the number of the sample.

Metric	Equation	Unit
PCC	$PCC = \frac{\sum_{i=1}^n (P_i - \bar{P})(M_i - \bar{M})}{\sqrt{\sum_{i=1}^n (P_i - \bar{P})^2 \sum_{i=1}^n (M_i - \bar{M})^2}}$	—
RMSE	$RMSE = \sqrt{\frac{\sum_{i=1}^n (P_i - M_i)^2}{n}}$	°C
bias	$bias = \frac{1}{n} \sum_{i=1}^n (P_i - M_i)$	°C
MAE	$MAE = \frac{1}{n} \sum_{i=1}^n P_i - M_i $	°C

4. Results

4.1. Correlation Analysis for Dependent and Independent Variables

First, Pearson correlation coefficient (PCC) was adopted to investigate the relationship between in-situ average temperature and each predictor. The result is presented in Figure 4. It can be seen that in-situ temperature indicated strong positive relationship with land surface temperature and ERA-5 temperature with PCC of 0.91 and 0.95, respectively. To this point, the inputs of LST and model-based temperature might be beneficial to the improvement of accuracy for the downscaled temperature, which have also been confirmed in some previous studies. Besides, in-situ temperature also showed moderate positive correlation with NDVI (0.40) and negative correlations with elevation (−0.44) and Albedo (−0.38). For SSM, wind speed, and DOY, only weak correlations were observed with absolute PCC lower than 0.3.

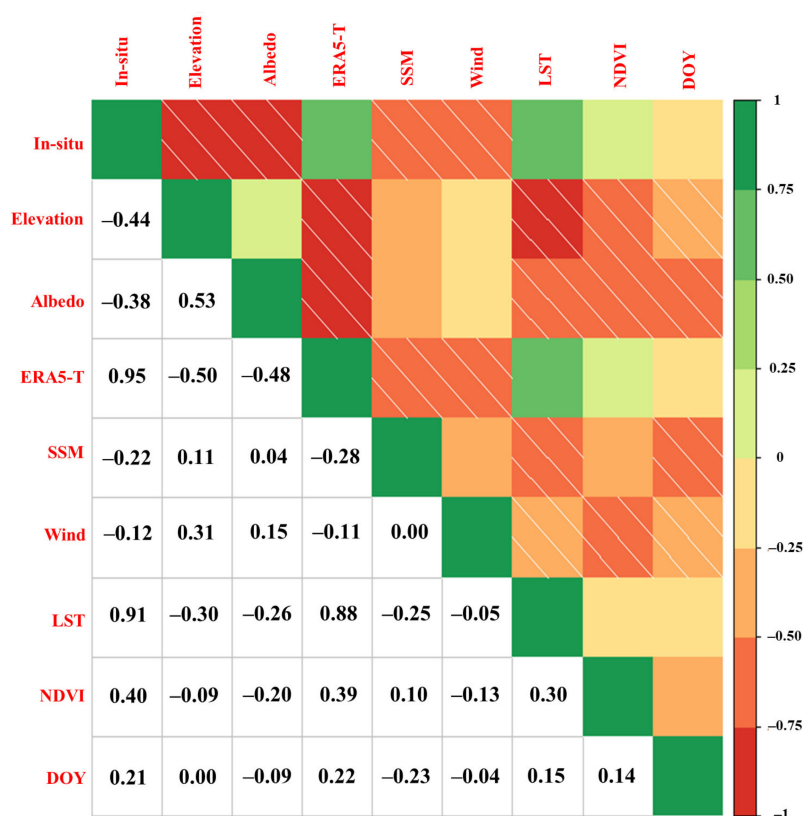


Figure 4. The correlation coefficient between air temperature and each predictor variables. The blue color represents positive relationship while the red color means negative relationship. The lower triangle of the figure represents the specific PCC values between two variables while the upper triangle uses colors and oblique lines to represent the positive or negative relationship.

4.2. Performance of the Downscaled Temperature

4.2.1. Evaluation of the Performance at Validation Sites

By combining the eight aforementioned input variables, the DBN based downscaling model was constructed from January 1st to December 31th during 2019. The entire sample set was divided into training set, validation set, and test set following the ratio of 7:2:1. Therefore, a total of 20 meteorological stations were randomly selected for the validation of downscaling performance. To evaluate the predictive power of DBN model in downscaling average air temperature, firstly, we plotted the scatter density plots for the 20 validation sites (Figure 5). The x and y axes represent in-situ and downscaled temperature, respectively while the red color indicates the dense concentration of scatter points. In general, the scatter points for all validation sites were concentrated near the 1:1 line which illustrated that the downscaled temperature showed high consistence with in-situ ground measurements. Specifically, the downscaled temperature exhibited strong correlation with in-situ ground observations with PCC values generally higher than 0.94 for all validation stations while RMSE was ranging from 1.13 °C to 3.69 °C. The average PCC, RMSE, and bias for these validation sites achieved 0.983 °C, 1.96 °C, and 1.57 °C, respectively. Results demonstrated that DBN model showed excellent performance in downscaling temperature with 1 km spatial resolution at relatively high accuracy.

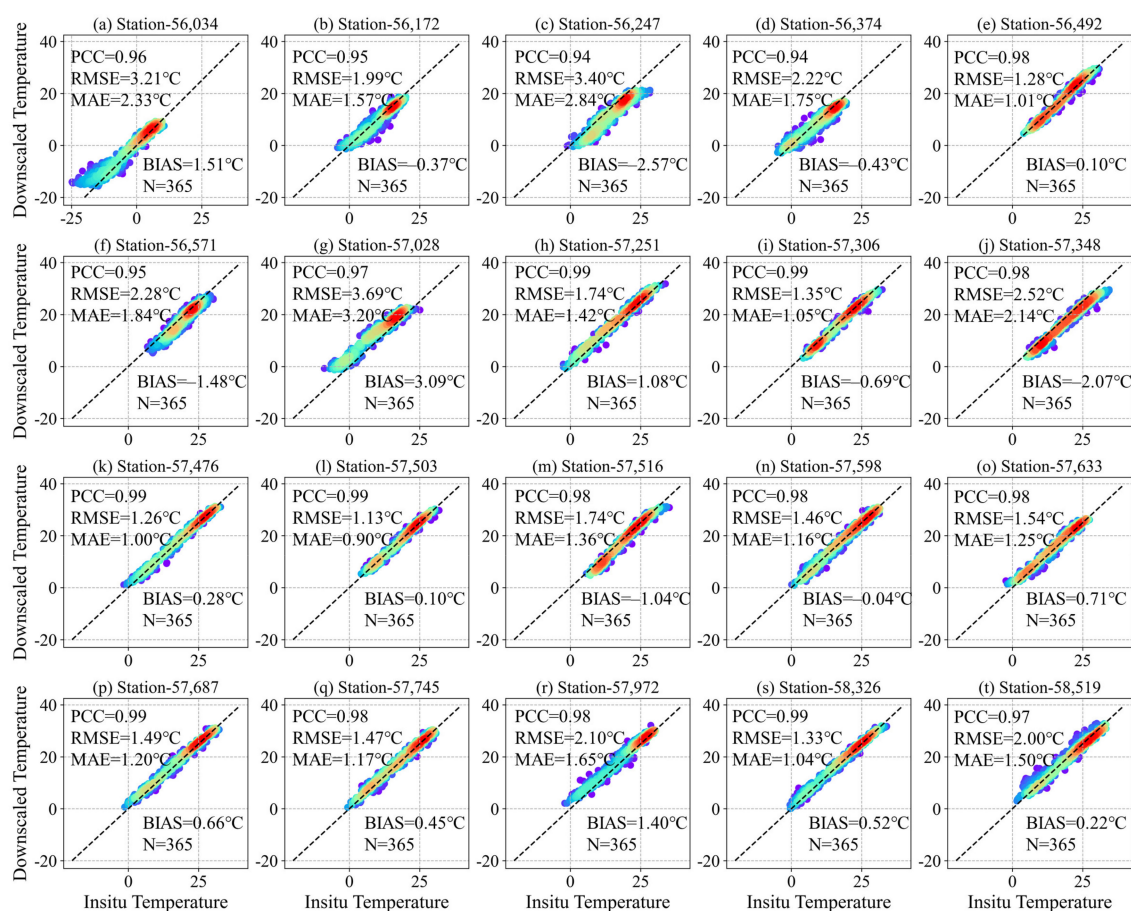


Figure 5. The scatter density plots and statistical metrics for 20 validation stations. The x and y axes represent in-situ ground measurements and downscaled temperature, respectively. The red color represents dense concentration of scatters. N means the number of observations for validation.

However, it can be observed that the distribution of density scatter points still varied from stations to stations. For instance, station 56,034 and 57,028 represented obvious overestimation against in-situ ground data while station 56,247 and 57,348 showed underestimation compared to in-situ observations. To further investigate the spatial patterns of the statistical metrics and downscaling accuracy in all meteorological stations, the distributions of four metrics are presented in Figure 6. Prominent spatial variations of these statistical metrics can be observed from the figure. For PCC, RMSE, and MAE, the stations located in the middle and lower region of YRB exhibited significantly higher accuracy (i.e., higher PCC values and lower RMSE and MAE) than that of upper reach. It may attribute to the complicated terrain in the west of YRB. The topography of upper region of YRB are mainly dominated by mountains and plateaus. And typical topographical areas include Qinghai-Tibet Plateau, Hengduan Mountains, Yunnan-Guizhou Plateau, and Sichuan Basin, which form a huge drop in elevation. Previous studies have found that the accuracy of some existing temperature products was relatively low in these areas, which was in line with the results of our study [30].

4.2.2. Spatio-Temporal Analysis of the Downscaled Temperature

A reliable temperature downscaling framework is supposed to achieve two benchmarks. First, the downscaled temperature is required to capture the temporal variation of in-situ ground observations (which are regarded as true values here). Second, the downscaled temperature should reconstruct the original spatial patterns of temperature in the study area. In order to evaluate whether the proposed temperature downscaling

framework can satisfy these two criteria, we conduct validation analysis from both spatial and temporal perspectives.

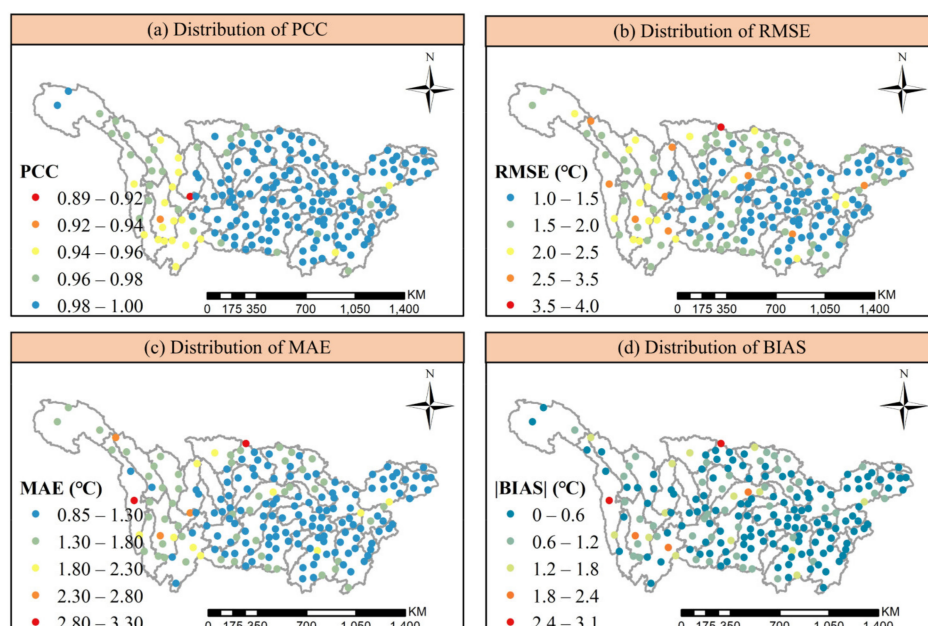


Figure 6. The spatial distribution of statistical metrics for 20 validation sites in YRB. (a–d) represent the distribution of PCC, RMSE, MAE, and bias.

To examine the capability of capturing temporal dynamics for the downscaled temperature, a total of six validation stations were randomly selected. The temporal variations of downscaled temperature (red dashed line), in-situ ground observations (purple point), and ERA-5 temperature (orange line) at these stations are shown in Figure 7. In general, the downscaled temperature represented higher consistence with in-situ measurements rather than ERA-5 temperature. ERA-5 temperature showed more overestimation or underestimation against in-situ observations, which could be significantly observed in station 56,374 and 57,687. It is mainly attributed to the fact that the spatial scale heterogeneity between ground measurement and satellite-retrieved data is often existed. Although some errors also existed in downscaled temperature at some time, the overall trend of temperature variations could be well monitored and captured by applying DBN model. Results further indicated the effectiveness of the proposed downscaling framework for generating high quality temperature data.

Here we also compared the spatial distribution of our downscaled temperature with that of the model-based ERA-5 temperature (Figure 8). The hourly ERA-5 temperature had been merged to daily temperature in this case. From the figure, the spatial pattern of temperature data downscaled by DBN model shared some similarities with the ERA-5 temperature. It indicated that the DBN based downscaling model could will capture the overall spatial trend of temperature in YRB. Additionally, the downscaled temperature exhibited more spatial details than the model-based temperature. For example, more detailed spatial variations can be observed in the southwestern and middle areas in YRB in the downscaled temperature data than the assimilated temperature product. In a word, the proposed downscaling framework successfully generated 1 km spatially seamless and temporally continuous temperature by applying point-surface data fusion method and DBN model.

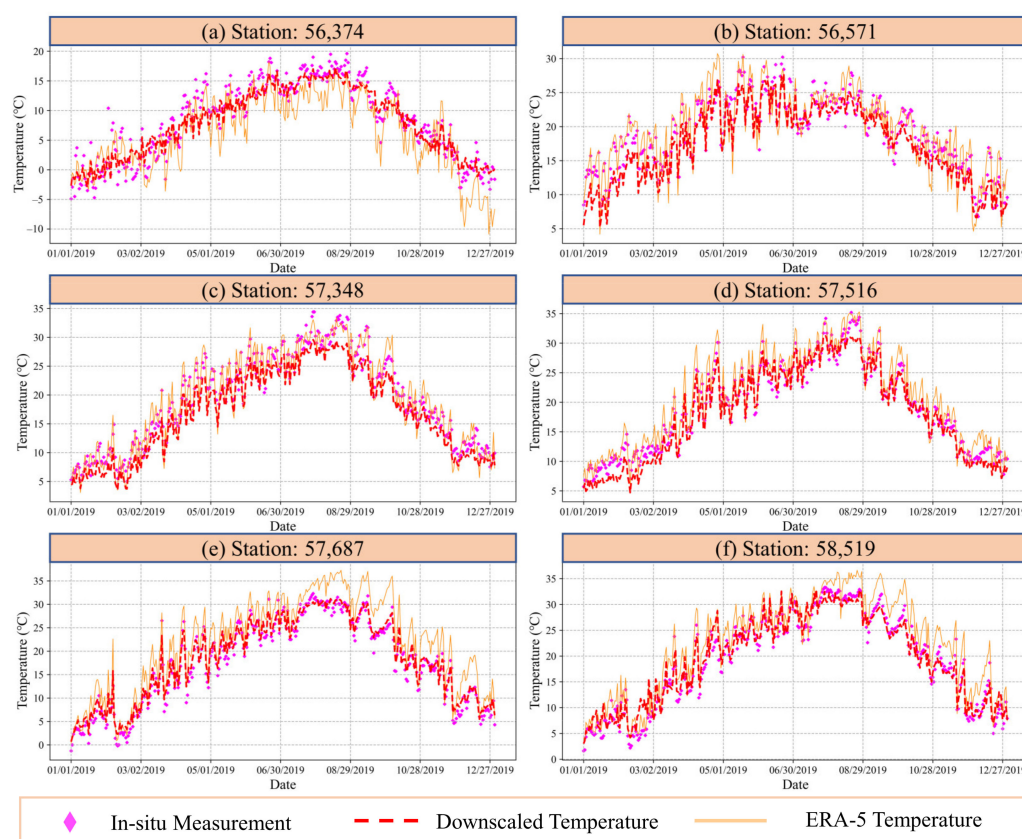


Figure 7. The temporal variations of the temperature data in 2019 at six randomly selected stations. The purple points represent in-situ ground measurements while the red dashed line and orange line indicate the downscaled temperature and ERA-5 temperature, respectively.

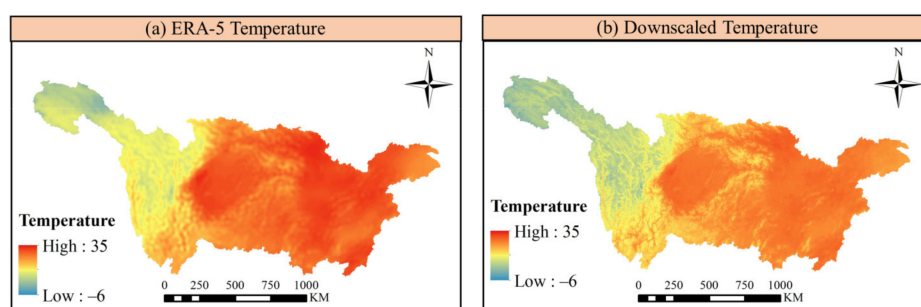


Figure 8. The spatial distribution of ERA-5 temperature and downscaled temperature in 1 July in YRB.

Moreover, we mapped the spatial distributions of average downscaled temperature in each season in 2019 (Figure 9). The spatial patterns of downscaled temperature showed prominent seasonality and spatial heterogeneity in YRB. The overall temperature ranged from -23°C to 30°C in 2019. Temporally, average temperature was significantly higher in summer (June to August) and lower in winter (December to February). Spatially, the downscaled temperature increased from the western YRB to the middle and lower regions of YRB. Location with lowest temperature lay in the Qinghai-Tibet Plateau, which had the highest elevation in the entire YRB.

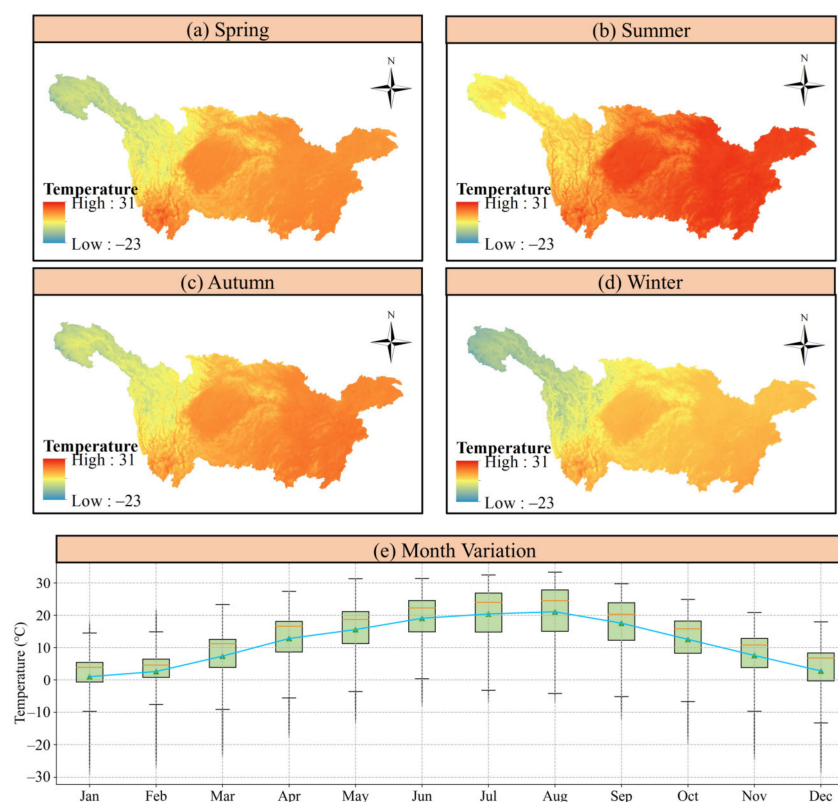


Figure 9. The spatial distributions of average downscaled temperature during each season in 2019. (a–d) are the spatial distributions of downscaled temperature in four seasons. (e) exhibits the temporal variation of downscaled temperature in each month.

4.3. Assessment of the Calibrated Temperature

Although previous downscaling procedure had successfully generated 1 km seamless and continuous temperature, underestimation or overestimation still existed in some periods. In order to further improve the accuracy of downscaled temperature and achieve the 3H goal, we adopted GRA and GDA calibration methods which considered the ratio and difference between downscaled and observed temperature, respectively. The calibration methods were evaluated over 20 validation stations and the remaining sites were used to calculate the calibration parameters. The statistical metrics for the 20 validation sites before and after the calibration are shown in Figure 10. In general, PCC values increased after the bias correction while the RMSE, bias, and MAE decreased. To be specific, the GDA method exhibited more significant improvement in downscaling accuracy compared to GRA. Although GRA generally improved the accuracy, it should be noted that it may also cause opposite calibration due to the fact that temperature has negative values which will influence the sign of the calibration parameters. GRA is more suitable for the variables which are constantly positive or negative. In this case, GDA was more suitable for the bias calibration since GDA applied add operation rather than multiply. In a word, after the GDA calibration, the average PCC, RMSE, and MAE achieved 0.987, 1.54 °C, and 1.25 °C which improved about 0.4%, 21.42%, and 20.38%, respectively.

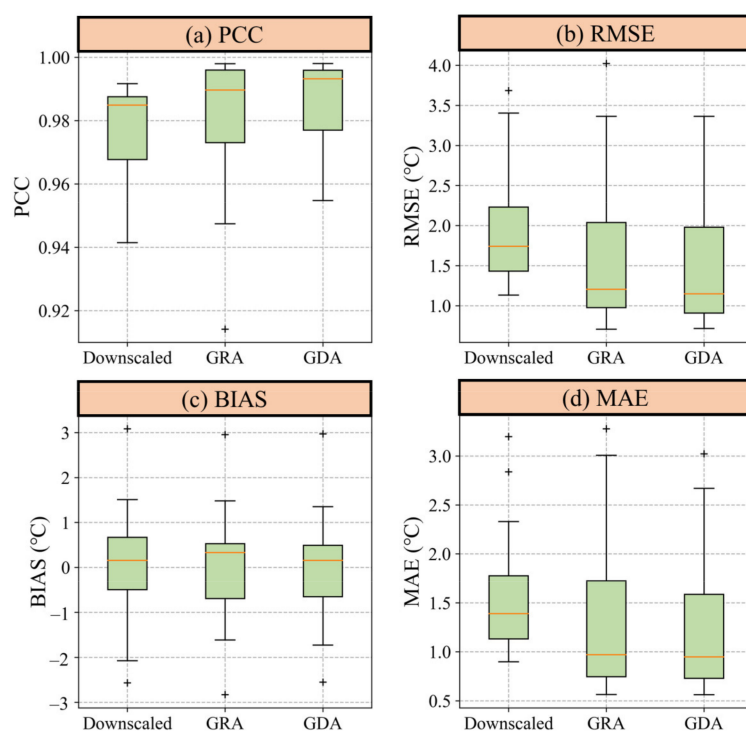


Figure 10. The box plots of the statistical metrics for 20 validation stations. Boxes from left to right in each subplot represent downscaled temperature, calibrated temperature by GRA, and calibrated temperature by GDA, respectively.

The spatial distributions of the temperature before and after GDA calibration are also presented in Figure 11. From Figure 11b, the residuals between downscaled temperature and ground observations ranged from -3°C to 3°C . Results indicated that overestimation of temperature mainly concentrated in the middle region of YRB while underestimation usually concentrated in the southwestern areas.

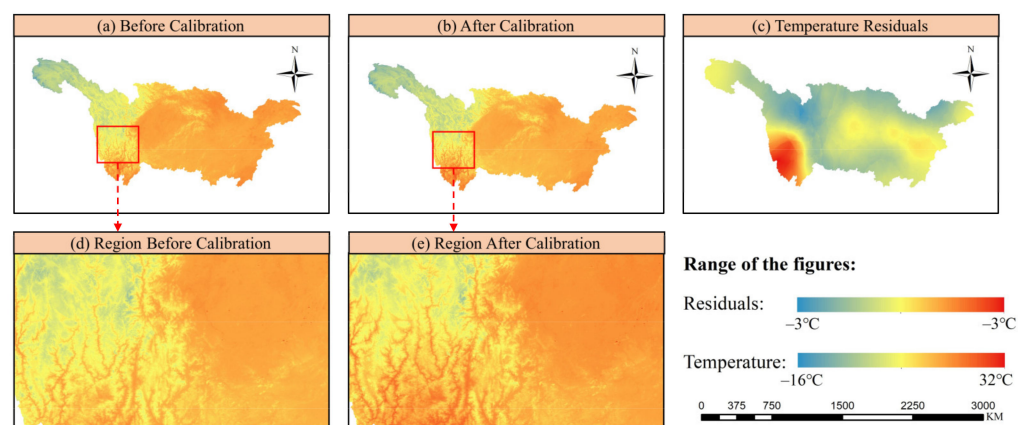


Figure 11. The spatial distribution of downscaled temperature before (a) and after (b) bias calibration. (c) is the distribution of residuals between downscaled temperature and in-situ observations. (d,e) are the regions with significant changes before and after calibration.

Based on the aforementioned analysis, the proposed temperature downscaling framework combining point-surface data fusion, deep learning, and bias calibration finally achieved best performance in generating 1 km spatially seamless and temporally continuous temperature. The average PCC, RMSE, and MAE after calibration achieved 0.987,

1.54 °C, and 1.25 °C, which satisfied the goal of producing high accuracy data and confirmed the effectiveness of the downscaling framework.

5. Discussion

5.1. Spatio-Temporal Evaluation of the Downscaling Accuracy

To investigate the performance of downscaling framework in different months, Figure 12 presents the variations of statistical metrics for all validation sites in month scale. The blue line indicates the mean value of corresponding metric. Generally, the variations of downscaling accuracy also represented distinct differences in different months. Specifically, downscaled temperature in spring (March to May) and autumn (September to November) showed lower errors rather than that in summer and winter. February and December witnessed relatively low downscaling accuracy with average PCC values of 0.69 and 0.60.

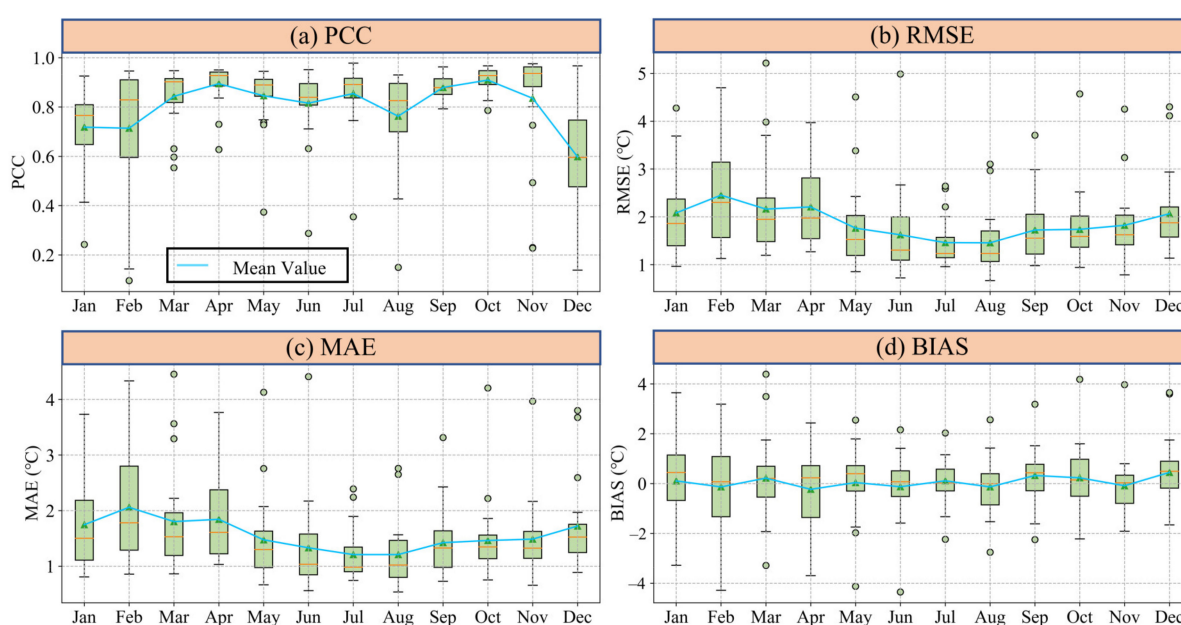


Figure 12. The temporal variations of PCC, RMSE, MAR, and bias in each month. The blue line represents the variations of mean value for each statistical metric.

Additionally, we also examined the downscaling accuracy in diverse land cover types including grassland, water, forest, farmland, and building. Results of the metrics are shown in Figure 13. It can be seen that water and building areas had relatively good performance with average RMSE of 1.32 °C and 1.51 °C, respectively. However, DBN model performed relatively weaker in grassland and farmland with RMSE up to 1.89 °C and 1.64 °C. Besides, it is also widely acknowledged that air temperature is highly correlated to the elevation, of which the temperature will decrease with the increase of elevation. To this point, to what extent the elevation affected the temperature downscaling accuracy was also worthy to explore. Figure 13b classifies the elevation into five levels with an interval of 1000 m. The statistical metrics varied in different ranges of elevation. Generally, the DBN performance was weakened with the increase of elevation. However, it is noteworthy that for the elevation over 3000 m, the model performance represented as an opposite trend (i.e., performed relatively better).

5.2. Comparison for Different Downscaling Algorithms

In the field of data fusion, spatial statistical methods (e.g., geographical weighted regression) and machine learning algorithms have been widely adopted to downscale and predict land surface variables. The commonly used machine learning approaches include random forest (RF), back-propagation neural network (BPNN), support vector

machine (SVM), and gradient boosting decision tree (GBDT). With the rising of deep learning, researchers have also started to focus on the application of deep learning models in earth science studies [55]. For instance, Wu et al. [56] combined convolutional neural network (CNN) and long-short-term memory network (LSTM) to downscale high accuracy precipitation with a spatial resolution of 0.05° . Li et al. [57] developed a geo-intelligent deep belief network to map $PM_{2.5}$ in China. In this study, we adopted deep learning model to downscale 1 km seamless and continuous temperature. To evaluate the role of deep learning in the downscaling framework, we also conducted to comparative experiments using other competing deep learning and machine learning algorithms, including long short-term memory network (LSTM), BPNN, RF, classification and regression trees (CART), and SVM. The automated machine learning (AutoML) technique was also adopted to help the construction of machine learning models, which has been widely used in various fields [58]. The effectiveness of these downscaling has been confirmed in various previous studies. The results of four statistical metrics averaging for 20 validation stations are shown in Figure 14. In general, all of these methods can achieve acceptable results in downscaling temperature. In comparison, three neural network models (i.e., DBN, LSTM, and BPNN) and RF outperformed CART and SVM with PCC values higher than 0.96 and RMSE lower than 2.25°C . Among the first four algorithms, BPNN had poorest performance with PCC, RMSE, MAE of 0.965, 2.25°C , and 1.68°C , respectively. Random forest showed slightly better predictive power than BPNN. Generally, it can be observed that deep learning methods (i.e., DBN and LSTM) represented better capability than other machine learning models in downscaling temperature. The results indicated that DBN exhibited most powerful downscaling performance for obtaining the lowest errors (i.e., PCC, RMSE, MAE of 0.983, 1.96°C , and 1.57°C) against in-situ observations. It was largely attributed to the parameter initialization in the pre-training of RBM model, which overcomes the disadvantages of random initialization of traditional BPNN that may induce falling into the local optima and consuming long training time. The pre-training step can be regarded as the parameter initialization for a deep BPNN. Overall, the comparative analysis further confirmed the effectiveness of DBN in the proposed downscaling framework for producing high accuracy temperature data.

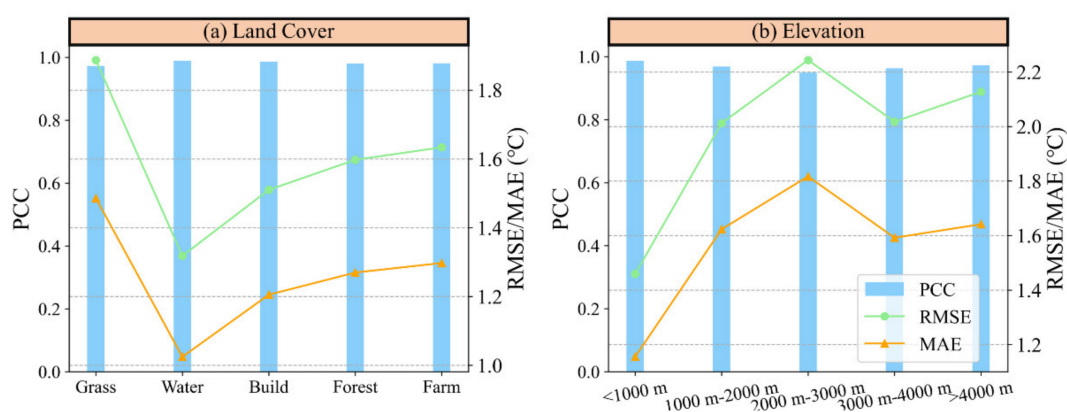


Figure 13. Model performance in different land cover types (grassland, farmland, forest, building, and water) and ranges of elevation (<1000 m, 1000~2000 m, 2000~3000 m, 3000~4000 m, >4000 m). The blue, orange, and green colors represent PCC, MAE, and RMSE, respectively.

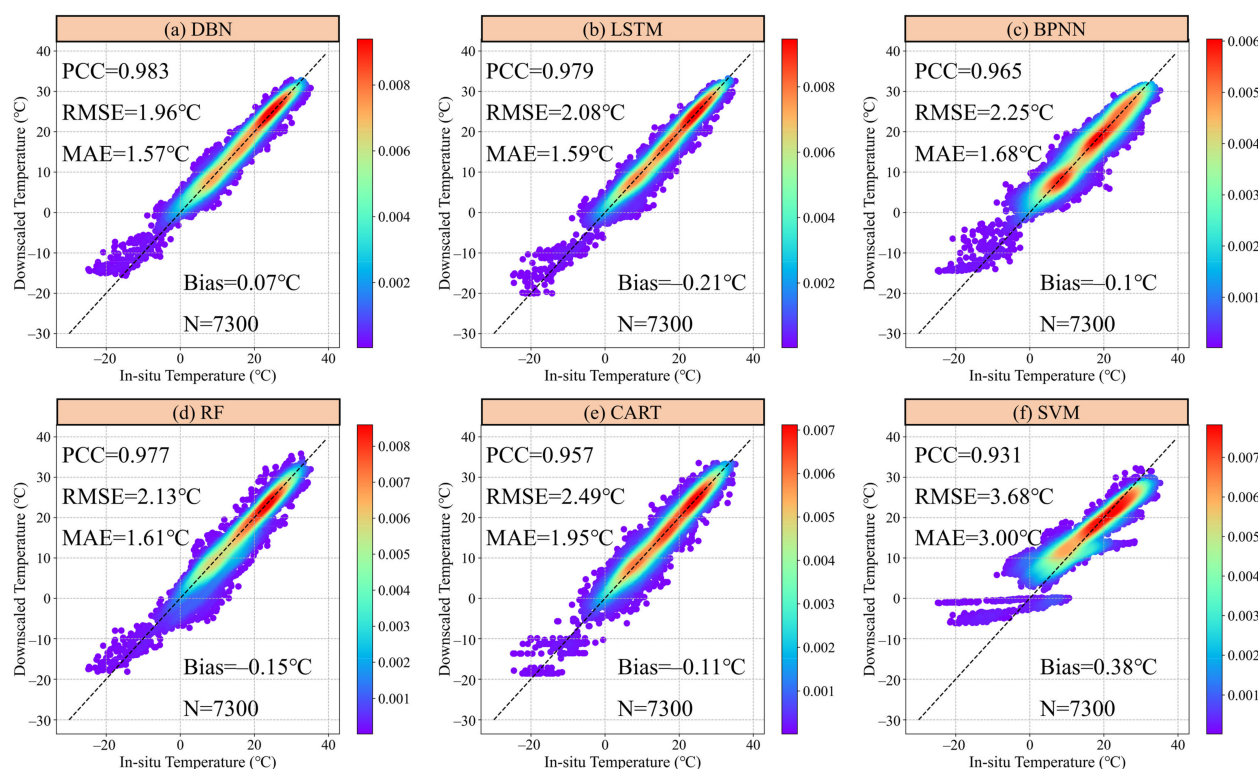


Figure 14. The comparative analysis of six downscaling algorithms in generating 3H temperature. (a–f) represent the performance of DBN, LSTM, BPNN, RF, CART, and SVM on 20 validation station, respectively.

5.3. Role of Point-Surface Fusion in Generating 3H Temperature Data

In this study, we applied point-surface data fusion in downscaling temperature since in-situ ground measurements are usually considered the most accurate compared to other data sources such as satellite-based and model-based products [59,60]. Some previous downscaling studies used remotely sensed or assimilated products as model outputs, which failed to take full advantages of in-situ ground observations. In order to determine and evaluate the role of point-surface data fusion in improving the downscaling accuracy, we set a comparative experiment by applying a surface-surface fusion method in temperature downscaling. In this case, the output of the DBN model was ERA-5 temperature instead of in-situ measurements. The density scatter plots for 20 validation stations are presented in Figure 15. Compared to the downscaled temperature using model-based temperature as output, the accuracy of the downscaled temperature by adopting ground observations as output was substantially improved. The average PCC increased from 0.94 to 0.98 while the RMSE, MAE raised from 3.71 °C and 2.98 °C to 1.96 °C and 1.57 °C, which decreased about 47.17% and 47.32%, respectively. Although downscaled temperature in the case of surface-surface fusion still maintained high correlation with in-situ measurements, it is mostly attributed to the originally high correlation between ERA-5 temperature and ground observations. In a word, the application of point-surface data fusion was proved to enhance the overall performance of DBN model in generating 3H temperature.

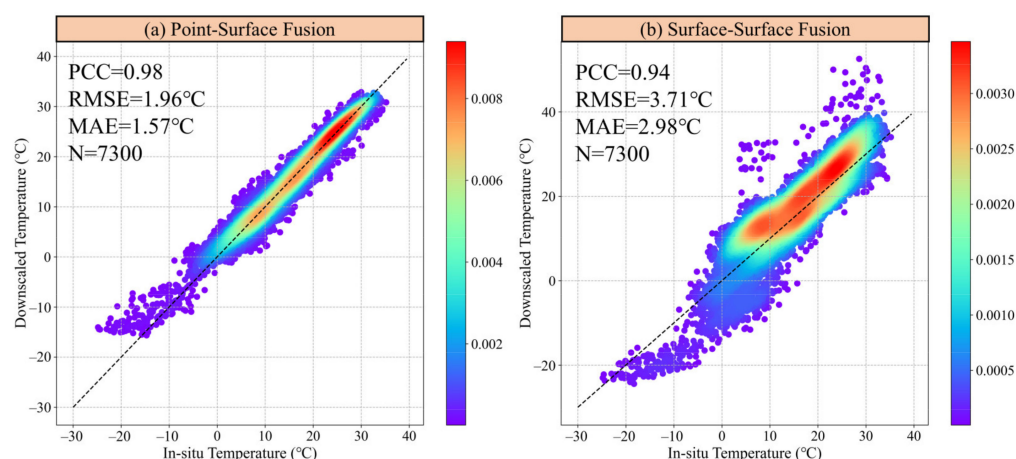


Figure 15. The scatter density plots for 20 validation stations based on point-surface data fusion (a) and surface-surface data fusion (b).

6. Conclusions

In this study, we proposed an integrated temperature downscaling framework inspired by point-surface data fusion through deep learning. The downscaling framework was applied to generate high resolution (1 km), high spatio-temporal continuity (spatially seamless and daily), and high accuracy temperature data over the Yangtze River Basin in 2019 by fusing remotely sensed, assimilated, and station-based products. Compared with conventional data fusion algorithms (e.g., RF, BPNN), deep learning exhibited excellent performance in downscaling air temperature. The average PCC, RMSE, MAE, and bias for the 20 validation stations achieved 0.983, 1.96 °C, 1.57 °C, and 0.07 °C, respectively. In order to further enhance the model performance, GRA and GDA calibration methods were applied by integrating in-situ ground measurements. Results demonstrated that GDA had better capability in improving downscaling accuracy than GRA. Specifically, PCC values increased from 0.983 to 0.987 while RMSE and MAE were decreased by 21.42% and 20.38%, respectively. The comparison between point-surface fusion and surface-surface fusion also indicated that the combination of station-based data could greatly improve the downscaling accuracy, which decreased the RMSE and MAE about 47.17% and 47.32%. To conclude, the results and comparative analysis confirmed that the proposed temperature downscaling framework had potential to generate 3H temperature data, which would be of great significance for global warming and climate change assessment as well as hydrology, agriculture, and public health management.

Author Contributions: Conceptualization, S.H. and R.L.; methodology, S.H. and R.L.; software, S.H.; validation, S.H., T.H. and Y.S.; formal analysis, X.Z. and S.H.; investigation, R.L. and S.H.; resources, S.H. and R.L.; data curation, T.H. and Y.S.; writing—original draft preparation, S.H. and R.L.; writing—review and editing, S.H. and X.Z.; visualization, S.H. and R.L.; supervision, X.Z.; project administration, X.Z. All authors have read and agreed to the published version of the manuscript.

Funding: This work was funded by grants from the National Key R&D Program (no.2018YFB2100500) and National Natural Science Foundation of China program (41801339, 41890822, 41771422, 41601406).

Institutional Review Board Statement: Not applicable.

Informed Consent Statement: Not applicable.

Data Availability Statement: The NDVI from MOD13A2 can be obtained at <https://lpdaac.usgs.gov/products/mod13a2v006/> (accessed on 15 June 2021). TRIMS LST is available at <https://data.tpdc.ac.cn/en/data/05d6e569-6d4b-43c0-96aa-5584484259f0/> (accessed on 17 June 2021). ERA-5 reanalysis product can be accessed at <https://www.ecmwf.int/en/forecasts/datasets/reanalysis-datasets/era5> (accessed on 17 June 2021). The SRTM data can be obtained at <https://lpdaac.usgs.gov/tools/appears/> (accessed on 18 June 2021). The in-situ meteorological data is available at <http://data.cma.cn/> (accessed on 21 April 2021). The source code of this paper can be found at <https://github.com/hsz602432385/Temperature-Downscaling> (accessed on 18 June 2021).

Acknowledgments: The authors would like to thank the editors and two anonymous reviewers for their constructive suggestions and comments.

Conflicts of Interest: The authors declare no conflict of interest.

References

- Wang, L.; Koike, T.; Yang, K.; Yeh, P.J.-F. Assessment of a distributed biosphere hydrological model against streamflow and MODIS land surface temperature in the upper Tone River Basin. *J. Hydrol.* **2009**, *377*, 21–34. [\[CrossRef\]](#)
- Lin, S.; Moore, N.J.; Messina, J.P.; DeVisser, M.H.; Wu, J. Evaluation of estimating daily maximum and minimum air temperature with MODIS data in east Africa. *Int. J. Appl. Earth Obs. Geoinf.* **2012**, *18*, 128–140. [\[CrossRef\]](#)
- Qin, W.; Yan, H.; Zou, B.; Guo, R.; Ci, D.; Tang, Z.; Zou, X.; Zhang, X.; Yu, X.; Wang, Y.; et al. Arbuscular mycorrhizal fungi alleviate salinity stress in peanut: Evidence from pot-grown and field experiments. *Food Energy Secur.* **2021**, e34. [\[CrossRef\]](#)
- Pepin, N.; Bradley, R.S.; Diaz, H.F.; Baraer, M.; Caceres, E.B.; Forsythe, N.; Fowler, H.; Greenwood, G.; Hashmi, M.Z.; Liu, X.D.; et al. Elevation-dependent warming in mountain regions of the world. *Nat. Clim. Chang.* **2015**, *5*, 424–430. [\[CrossRef\]](#)
- Zhang, X.; Chen, N.; Li, J.; Chen, Z.; Niyogi, D. Multi-sensor integrated framework and index for agricultural drought monitoring. *Remote Sens. Environ.* **2017**, *188*, 141–163. [\[CrossRef\]](#)
- Gu, X.; Zhang, Q.; Li, J.; Singh, V.P.; Liu, J.; Sun, P.; Cheng, C. Attribution of Global Soil Moisture Drying to Human Activities: A Quantitative Viewpoint. *Geophys. Res. Lett.* **2019**, *46*, 2573–2582. [\[CrossRef\]](#)
- Gu, X.; Zhang, Q.; Li, J.; Singh, V.P.; Liu, J.; Sun, P.; He, C.; Wu, J. Intensification and Expansion of Soil Moisture Drying in Warm Season Over Eurasia Under Global Warming. *J. Geophys. Res. Atmos.* **2019**, *124*, 3765–3782. [\[CrossRef\]](#)
- Chen, D.; Chen, N.; Xiang, Z.; Ma, H.; Chen, Z. Next-Generation Soil Moisture Sensor Web: High Density In-situ Observation over NB-IoT. *IEEE Internet Things J.* **2021**. [\[CrossRef\]](#)
- Chen, N.; Zhang, X.; Wang, C. Integrated open geospatial web service enabled cyber-physical information infrastructure for precision agriculture monitoring. *Comput. Electron. Agric.* **2015**, *111*, 78–91. [\[CrossRef\]](#)
- Kobayashi, S.; Ota, Y.; Harada, Y.; Ebata, A.; Morioka, M.; Onoda, H.; Onogi, K.; Kamahori, H.; Kobayashi, C.; Endo, H.; et al. The JRA-55 Reanalysis: General Specifications and Basic Characteristics. *J. Meteorol. Soc. Jpn.* **2015**, *93*, 5–48. [\[CrossRef\]](#)
- Rodell, M.; Houser, P.R.; Jambor, U.; Gottschalk, J.; Mitchell, K.; Meng, C.J.; Arsenault, K.; Cosgrove, B.; Radakovitch, J.; Bosilovich, M.; et al. The Global Land Data Assimilation System. *Bull. Am. Meteorol. Soc.* **2004**, *85*, 381–394. [\[CrossRef\]](#)
- Kanamitsu, M.; Ebisuzaki, W.; Woollen, J.; Yang, S.-K.; Hnilo, J.J.; Fiorino, M.; Potter, G.L. NCEP-DOE AMIP-II Reanalysis (R-2). *Bull. Am. Meteorol. Soc.* **2002**, *83*, 1631–1644. [\[CrossRef\]](#)
- Hersbach, H.; Bell, B.; Berrisford, P.; Hirahara, S.; Horányi, A.; Muñoz-Sabater, J.; Nicolas, J.; Peubey, C.; Radu, R.; Schepers, D.; et al. The ERA5 global reanalysis. *Q.J.R. Meteorol. Soc.* **2020**, *146*, 1999–2049. [\[CrossRef\]](#)
- Luo, M.; Liu, T.; Frankl, A.; Duan, Y.; Meng, F.; Bao, A.; Kurban, A.; De Maeyer, P. Defining spatiotemporal characteristics of climate change trends from downscaled GCMs ensembles: How climate change reacts in Xinjiang, China. *Int. J. Climatol.* **2018**, *38*, 2538–2553. [\[CrossRef\]](#)
- Wang, F.; Tian, D.; Lowe, L.; Kalin, L.; Lehrter, J. Deep Learning for Daily Precipitation and Temperature Downscaling. *Water Resour. Res.* **2021**, *57*. [\[CrossRef\]](#)
- Zhang, F.; Zhang, H.; Hagen, S.C.; Ye, M.; Wang, D.; Gui, D.; Zeng, C.; Tian, L.; Liu, J. Snow cover and runoff modelling in a high mountain catchment with scarce data: Effects of temperature and precipitation parameters. *Hydrol. Process.* **2015**, *29*, 52–65. [\[CrossRef\]](#)
- Immerzeel, W.W.; Petersen, L.; Ragettli, S.; Pellicciotti, F. The importance of observed gradients of air temperature and precipitation for modeling runoff from a glacierized watershed in the Nepalese Himalayas. *Water Resour. Res.* **2014**, *50*, 2212–2226. [\[CrossRef\]](#)
- Zhang, L.; Xu, Y.; Meng, C.; Li, X.; Liu, H.; Wang, C. Comparison of Statistical and Dynamic Downscaling Techniques in Generating High-Resolution Temperatures in China from CMIP5 GCMs. *J. Appl. Meteorol. Climatol.* **2020**, *59*, 207–235. [\[CrossRef\]](#)
- Rummukainen, M. State-of-the-art with regional climate model. *Wiley Interdiscip. Rev. Clim. Chang.* **2010**, *1*, 82–96. [\[CrossRef\]](#)
- Holden, Z.A.; Abatzoglou, J.T.; Luce, C.H.; Baggett, L.S. Empirical downscaling of daily minimum air temperature at very fine resolutions in complex terrain. *Agric. For. Meteorol.* **2011**, *151*, 1066–1073. [\[CrossRef\]](#)
- Zhou, X.; Huang, G.; Wang, X.; Cheng, G. Dynamically-downscaled temperature and precipitation changes over Saskatchewan using the PRECIS model. *Clim. Dyn.* **2017**, *50*, 1321–1334. [\[CrossRef\]](#)
- Hou, P.; Chen, Y.; Qiao, W.; Cao, G.; Jiang, W.; Li, J. Near-surface air temperature retrieval from satellite images and influence by wetlands in urban region. *Theor. Appl. Climatol.* **2012**, *111*, 109–118. [\[CrossRef\]](#)

23. Mostovoy, G.V.; King, R.L.; Reddy, K.R.; Kakani, V.G.; Filippova, M.G. Statistical Estimation of Daily Maximum and Minimum Air Temperatures from MODIS LST Data over the State of Mississippi. *GISci. Remote Sens.* **2013**, *43*, 78–110. [\[CrossRef\]](#)
24. Ma, H.; Zeng, J.; Zhang, X.; Fu, P.; Zheng, D.; Wigneron, J.-P.; Chen, N.; Niyogi, D. Evaluation of six satellite- and model-based surface soil temperature datasets using global ground-based observations. *Remote Sens. Environ.* **2021**, *264*. [\[CrossRef\]](#)
25. Long, D.; Bai, L.; Yan, L.; Zhang, C.; Yang, W.; Lei, H.; Quan, J.; Meng, X.; Shi, C. Generation of spatially complete and daily continuous surface soil moisture of high spatial resolution. *Remote Sens. Environ.* **2019**, *233*, 111364. [\[CrossRef\]](#)
26. Shen, H.; Jiang, Y.; Li, T.; Cheng, Q.; Zeng, C.; Zhang, L. Deep learning-based air temperature mapping by fusing remote sensing, station, simulation and socioeconomic data. *Remote Sens. Environ.* **2020**, *240*, 111692. [\[CrossRef\]](#)
27. Li, X.; Zhou, Y.; Asrar, G.R.; Zhu, Z. Developing a 1 km resolution daily air temperature dataset for urban and surrounding areas in the conterminous United States. *Remote Sens. Environ.* **2018**, *215*, 74–84. [\[CrossRef\]](#)
28. Abbaszadeh, P.; Hamid, M.; Zhan, X. Downscaling SMAP Radiometer Soil Moisture over the CONUS Using an Ensemble Learning Method. *Water Resour. Res.* **2018**, *55*, 324–344. [\[CrossRef\]](#)
29. Liu, Y.; Jing, W.; Wang, Q.; Xia, X. Generating high-resolution soil moisture by using spatial downscaling techniques: A comparison of six machine learning algorithms. *Adv. Water Resour.* **2020**, *141*, 103601. [\[CrossRef\]](#)
30. Zhang, H.; Immerzeel, W.W.; Zhang, F.; de Kok, R.J.; Gorrie, S.J.; Ye, M. Creating 1-km long-term (1980–2014) daily average air temperatures over the Tibetan Plateau by integrating eight types of reanalysis and land data assimilation products downscaled with MODIS-estimated temperature lapse rates based on machine learning. *Int. J. Appl. Earth Obs. Geoinf.* **2021**, *97*. [\[CrossRef\]](#)
31. Rao, Y.; Liang, S.; Wang, D.; Yu, Y.; Song, Z.; Zhou, Y.; Shen, M.; Xu, B. Estimating daily average surface air temperature using satellite land surface temperature and top-of-atmosphere radiation products over the Tibetan Plateau. *Remote Sens. Environ.* **2019**, *234*, 111462. [\[CrossRef\]](#)
32. Mao, Q.; Peng, J.; Wang, Y. Resolution Enhancement of Remotely Sensed Land Surface Temperature: Current Status and Perspectives. *Remote Sens.* **2021**, *13*, 1306. [\[CrossRef\]](#)
33. Xu, J.; Zhang, F.; Jiang, H.; Hu, H.; Zhong, K.; Jing, W.; Yang, J.; Jia, B. Downscaling Aster Land Surface Temperature over Urban Areas with Machine Learning-Based Area-To-Point Regression Kriging. *Remote Sens.* **2020**, *12*, 1082. [\[CrossRef\]](#)
34. Xu, S.; Zhao, Q.; Yin, K.; He, G.; Zhang, Z.; Wang, G.; Wen, M.; Zhang, N. Spatial Downscaling of Land Surface Temperature Based on a Multi-Factor Geographically Weighted Machine Learning Model. *Remote Sens.* **2021**, *13*, 1186. [\[CrossRef\]](#)
35. Arshad, A.; Zhang, W.; Zhang, Z.; Wang, S.; Zhang, B.; Cheema, M.J.M.; Shalamzari, M.J. Reconstructing high-resolution gridded precipitation data using an improved downscaling approach over the high altitude mountain regions of Upper Indus Basin (UIB). *Sci. Total Environ.* **2021**, *784*, 147140. [\[CrossRef\]](#) [\[PubMed\]](#)
36. Xu, L.; Chen, N.; Moradkhani, H.; Zhang, X.; Hu, C. Improving Global Monthly and Daily Precipitation Estimation by Fusing Gauge Observations, Remote Sensing, and Reanalysis Data Sets. *Water Resour. Res.* **2020**, *56*, e2019WR026444. [\[CrossRef\]](#)
37. Reichstein, M.; Camps-Valls, G.; Stevens, B.; Jung, M.; Denzler, J.; Carvalhais, N.; Prabhat, M. Deep learning and process understanding for data-driven Earth system science. *Nature* **2019**, *566*, 195. [\[CrossRef\]](#)
38. Shen, C. A Transdisciplinary Review of Deep Learning Research and Its Relevance for Water Resources Scientists. *Water Resour. Res.* **2018**, *54*, 8558–8593. [\[CrossRef\]](#)
39. Li, X.; Zhang, K.; Gu, P.; Feng, H.; Yin, Y.; Chen, W.; Cheng, B. Changes in precipitation extremes in the Yangtze River Basin during 1960–2019 and the association with global warming, ENSO, and local effects. *Sci. Total Environ.* **2021**, *760*, 144244. [\[CrossRef\]](#)
40. Chen, J.; Gao, C.; Zeng, X.; Xiong, M.; Wang, Y.; Jing, C.; Krysanova, V.; Huang, J.; Zhao, N.; Su, B. Assessing changes of river discharge under global warming of 1.5 °C and 2 °C in the upper reaches of the Yangtze River Basin: Approach by using multiple-GCMs and hydrological models. *Quat. Int.* **2017**, *453*, 63–73. [\[CrossRef\]](#)
41. Stoll, M.J.; Brazel, A.J. Surface-Air Temperature Relationships in the Urban Environment of Phoenix, Arizona. *Phys. Geogr.* **2013**, *13*, 160–179. [\[CrossRef\]](#)
42. Tomlinson, C.J.; Chapman, L.; Thornes, J.E.; Baker, C.J.; Prieto-Lopez, T. Comparing night-time satellite land surface temperature from MODIS and ground measured air temperature across a conurbation. *Remote Sens. Lett.* **2012**, *3*, 657–666. [\[CrossRef\]](#)
43. Zhang, X.; Zhou, J.; Götsche, F.-M.; Zhan, W.; Shaomin, L.; Cao, R. A Method Based on Temporal Component Decomposition for Estimating 1-km All-Weather Land Surface Temperature by Merging Satellite Thermal Infrared and Passive Microwave Observations. *IEEE Trans. Geosci. Remote Sens.* **2019**, *57*, 4670–4691. [\[CrossRef\]](#)
44. Zhou, J.; Zhang, X.; Zhan, W.; Götsche, F.-M.; Liu, S.; Olesen, F.-S.; Hu, W.; Dai, F. A Thermal Sampling Depth Correction Method for Land Surface Temperature Estimation from Satellite Passive Microwave Observation Over Barren Land. *IEEE Trans. Geosci. Remote Sens.* **2017**, *55*, 4743–4756. [\[CrossRef\]](#)
45. Zhang, X.; Zhou, J.; Liang, S.; Wang, D. A practical reanalysis data and thermal infrared remote sensing data merging (RTM) method for reconstruction of a 1-km all-weather land surface temperature. *Remote Sens. Environ.* **2021**, *260*, 112437. [\[CrossRef\]](#)
46. Chen, J.; Jönsson, P.; Tamura, M.; Gu, Z.; Matsushita, B.; Eklundh, L. A simple method for reconstructing a high-quality NDVI time-series data set based on the Savitzky-Golay filter. *Remote Sens. Environ.* **2004**, *91*, 332–344. [\[CrossRef\]](#)
47. Jinhu, B.; Li, A.; Mengqiang, S.; Liqun, M.; Jiang, J. Reconstruction of NDVI time-series datasets of MODIS based on Savitzky-Golay filter. *J. Remote Sens.* **2010**, *14*, 725–741.
48. Savitzky, A.; Golay, M.J.E. Smoothing and Differentiation of Data by Simplified Least Squares Procedures. *Anal. Chem.* **1964**, *36*, 1627–1639. [\[CrossRef\]](#)

49. Li, T.; Shen, H.; Yuan, Q.; Zhang, X.; Zhang, L. Estimating Ground-Level PM_{2.5} by Fusing Satellite and Station Observations: A Geo-Intelligent Deep Learning Approach. *Geophys. Res. Lett.* **2017**, *44*, 11–985. [[CrossRef](#)]
50. Shen, H.; Li, T.; Yuan, Q.; Zhang, L. Estimating Regional Ground-Level PM_{2.5} Directly from Satellite Top-Of-Atmosphere Reflectance Using Deep Belief Networks. *J. Geophys. Res. Atmos.* **2018**, *123*. [[CrossRef](#)]
51. Hinton, G.; Osindero, S.; Teh, Y.-W. A Fast Learning Algorithm for Deep Belief Nets. *Neural Comput.* **2006**, *18*, 1527–1554. [[CrossRef](#)] [[PubMed](#)]
52. Piles, M.; Camps, A.; Vall-llossera, M.; Corbella, I.; Panciera, R.; Rudiger, C.; Kerr, Y.H.; Walker, J. Downscaling SMOS-Derived Soil Moisture Using MODIS Visible/Infrared Data. *IEEE Trans. Geosci. Remote Sens.* **2011**, *49*, 3156–3166. [[CrossRef](#)]
53. Cheema, M.J.M.; Bastiaanssen, W.G.M. Local calibration of remotely sensed rainfall from the TRMM satellite for different periods and spatial scales in the Indus Basin. *Int. J. Remote. Sens.* **2011**, *33*, 2603–2627. [[CrossRef](#)]
54. Duan, Z.; Bastiaanssen, W.G.M. First results from Version 7 TRMM 3B43 precipitation product in combination with a new downscaling-calibration procedure. *Remote Sens. Environ.* **2013**, *131*, 1–13. [[CrossRef](#)]
55. Yuan, Q.; Shen, H.; Li, T.; Li, Z.; Li, S.; Jiang, Y.; Xu, H.; Tan, W.; Yang, Q.; Wang, J.; et al. Deep learning in environmental remote sensing: Achievements and challenges. *Remote Sens. Environ.* **2020**, *241*, 111716. [[CrossRef](#)]
56. Wu, H.; Yang, Q.; Liu, J.; Wang, G. A spatiotemporal deep fusion model for merging satellite and gauge precipitation in China. *J. Hydrol.* **2020**, *584*, 124664. [[CrossRef](#)]
57. Li, T.; Shen, H.; Zeng, C.; Yuan, Q.; Zhang, L. Point-surface fusion of station measurements and satellite observations for mapping PM_{2.5} distribution in China: Methods and assessment. *Atmos. Environ.* **2016**, *152*, 477–489. [[CrossRef](#)]
58. He, X.; Zhao, K.; Chu, X. AutoML: A survey of the state-of-the-art. *Knowl.-Based Syst.* **2021**, *212*, 106622. [[CrossRef](#)]
59. Zhang, X.; Chen, N. Reconstruction of GF-1 Soil Moisture Observation Based on Satellite and In Situ Sensor Collaboration Under Full Cloud Contamination. *IEEE Trans. Geosci. Remote Sens.* **2016**, *54*, 5185–5202. [[CrossRef](#)]
60. Xu, L.; Chen, N.; Zhang, X.; Moradkhani, H.; Zhang, C.; Hu, C. In-situ and triple-collocation based evaluations of eight global root zone soil moisture products. *Remote Sens. Environ.* **2021**, *254*, 112248. [[CrossRef](#)]